magnetochemistry

MDPI

Communication

Slow Magnetic Relaxation in Unprecedented Mono-Dimensional Coordination Polymer of Ytterbium Involving Tetrathiafulvalene-Dicarboxylate Linker

Anjara Belio Castro [1], Julie Jung [1,2], Stéphane Golhen [1], Boris Le Guennic [1], Lahcène Ouahab [1], Olivier Cador [1] and Fabrice Pointillart [1,*]

[1] Institut des Sciences Chimiques de Rennes, UMR 6226 CNRS, Université de Rennes 1, 263 Avenue du Général Leclerc, 35042 Rennes Cedex, France; anjarabelio@gmail.com (A.B.C.); julie.jung@cec.mpg.de (J.J.); stephane.golhen@univ-rennes1.fr (S.G.); boris.leguennic@univ-rennes1.fr (B.L.G.); lahcene.ouahab@univ-rennes1.fr (L.O.); olivier.cador@univ-rennes1.fr (O.C.)

[2] Max-Planck-Institut für Chemische Energiekonversion, Stiftstraße 34-36, D-45470 Mulheim an der Ruhr, Germany

* Correspondence: fabrice.pointillart@univ-rennes1.fr; Tel.: +33223236752

Academic Editors: Marius Andruh and Liviu F. Chibotaru
Received: 31 March 2016; Accepted: 26 April 2016; Published: 11 May 2016

Abstract: A one-dimensional compound has been constructed through a Yb^{III} ion and bridging redox-active deprotonated 4,5-bis(carboxylic)-4′,5′-methyldithiotetrathiafulvene. This polymer displays slow magnetic relaxation due to the planar magnetic anisotropy of the Yb^{III}, which has been experimentally determined.

Keywords: single molecule magnets; lanthanide polymer; magnetic anisotropy; Ytterbium

1. Introduction

Since more than a decade, lanthanide ions are intensively used for the conception of single molecule magnets (SMM) [1]. These ions can be classified in two categories depending on the electron density distribution varying between planar (oblate) to axial (prolate) [2]. This is demonstrated by the numerous examples of Dy-based SMM [3] and, to a lesser extent, Yb-based SMM [4]. This SMM behavior is observed when the lanthanide ion is adequately coordinated to well-chosen ligands inducing specific ligand field and symmetry. In this way, the best candidates for each category are the oblate Dy^{III} ion when the ligand charge distribution is axial and the prolate Yb^{III} ion when this distribution is planar. Moreover lanthanide emission properties were recently exploited in this respect as a probe of the ligand field splitting in SMM [4–12]. The versatility of ligand chemistry allows adding one or more physical properties to the SMM behavior [13,14]. As well-known examples, tetrathiafulvalene (TTF) derivatives may display redox activity and electronic conductivity [15]. We previously demonstrated that the TTF-based ligands could play both the role of organic chromophore to sensitize the lanthanide luminescence, and of structural agent to favor the appearance of SMM behavior through magnetic isolation [12]. The TTF core was functionalized by several coordination groups [16,17] and, herein, we focus our attention on TTF-carboxylates and, specifically, on the 4,5-bis(carboxylic)-4′,5′-methyldithiotetrathiafulvene ($\mathbf{H_2L}$). To date, various 3d/4d/5d coordination compounds were built up from TTF-carboxylate ligands [18–25]. Nevertheless, examples with 4*f* elements are very rare and only concern zero-dimensionnal complexes [26,27]. In this communication, we report the first TTF-based lanthanide coordination polymer. The synthesis, single crystal X-ray structures, magnetic and optical properties of $\{[Yb(\mathbf{L})(H_2O)_3(DMF)]\cdot(\mathbf{HL})\cdot(H_2O)\}_n$ (DMF = dimethylformamide) are discussed.

2. Results and discussion

The {[Yb(**L**)$(H_2O)_3$(DMF)]· (**HL**)· (H_2O)}$_n$ (hereafter called **Yb**) polymer was obtained from the reaction of the Yb(hfac)$_3$· $2H_2O$ (hfac: hexafluoroacetylacetonate) metallic precursor and the disodium salt of **L** (**Na_2L**) in Dimethylformamide (DMF). It is worth noticing that, in the final **Yb** compound, no hfac$^-$ anion is found. The polymer cannot be obtained from either nitrate or halogenate salts of Yb^{III}. **Yb** crystallizes in the P-1 (No. 2) triclinic space group (Table S1). Each Yb^{III} ion is surrounded by eight oxygen atoms coming from four carboxylate groups (O1, O2 and O4, O5), three water molecules (O3, O6, O7) and one DMF molecule (O8) (Figure 1).

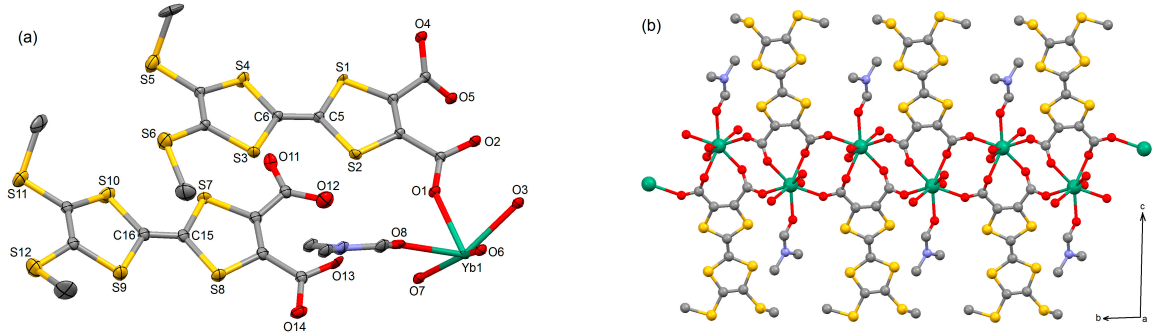

Figure 1. (**a**) Ortep view of the asymmetric unit of **Yb**. Thermal ellipsoids are drawn at 30% probability. Hydrogen atoms and water molecules of crystallization are omitted for clarity; and (**b**) representation of the one-dimensional structure running along the *b* axis.

The coordination polyhedron of the Yb^{III} can be described as a distorted square antiprism. The distortion is visualized by continuous shape measures performed with SHAPE 2.1 (0.454, D_{4d} symmetry) [28]. The two carboxylic functions of the TTF-based ligands which are linked to the metal remain fully deprotonated (**L^{2-}**) and bridge the metal ions in a $\mu_2(\eta_1, \eta_1)$ mode. The formed one-dimensional cationic complex runs along the *b* axis (Figure 1b). The electroneutrality of the edifice is guaranteed by non-coordinated mono-protonated ligands (**HL$^-$**) (drawn in green on the Figure S1a). In other words, the fully-deprotonated ligands **L^{2-}** play the role of bridges to form the mono-dimensional structure while the mono-deprotonated ligands **HL$^-$** play the role of anion to guarantee the neutrality of the crystal structure. An organic network is formed along the *a* axis through S···S short contacts (S2···S7 = 3.691 Å and S3···S7 = 3.646 Å) between the coordinated **L^{2-}** and uncoordinated **HL$^-$** anions (Figure 2). Short S···S contacts (S11···S11 = 3.462 Å and S12···S12 = 3.689 Å) are identified between the **HL$^-$** counter ions (Figure S1b). The water molecule of crystallization (O13W) generates a H-bond network that involves one oxygen atom of the coordinated carboxylate (O5, $d_{O13W\text{-}O5}$ = 2.951 Å), one oxygen atom of one non-coordinated carboxylic function (O12, $d_{O13W\text{-}O12}$ = 2.709 Å) and, finally, two coordinated water molecules (O3, $d_{O13W\text{-}O3}$ = 2.746 Å and O7, $d_{O13W\text{-}O7}$ = 2.748 Å).

The photophysical properties of **H_2L** (Figures S2a, S3 and Tables S2 and S3) and **Na_2L** (Figure S4 and Table S3) were investigated by absorption spectroscopy in CH_3OH solution and solid-state (KBr pellet). In the case of **H_2L**, the results are rationalized by DFT and TD-DFT calculations (see computational details; Figures S2b and S5, Table S2) [29]. For both protonated and deprotonated ligands, the lowest-energy absorption band is attributed to intra-ligand charge transfer (ILCT) and identified as HOMO → LUMO type excitation. At higher energy, the absorption bands mainly come from intra-donor (TTF) excitations (ID). Basically, the absorption spectrum of **Yb** in solid-state can be described as the addition of the absorption spectra of **Na_2L** and **H_2L** (Figure S6). No emission of the Yb^{III} ion was detected under irradiation on the ILCT band due to the presence of water molecules coordinated to the metal ion that are known to quench the luminescence [30].

The reversibility of the oxidation potentials and the redox-activity of **Yb** have been checked by cyclic voltametry. The cyclic voltamogram shows two mono-electronic oxidations at about 0.50 V and 0.85 V corresponding to the formation of a radical cation and a dication TTF fragment, respectively (Figure S7). No significant differences of oxidation potential values are detected between the coordinated $\mathbf{L}^{2-}$ and free $\mathbf{HL}^{-}$ species.

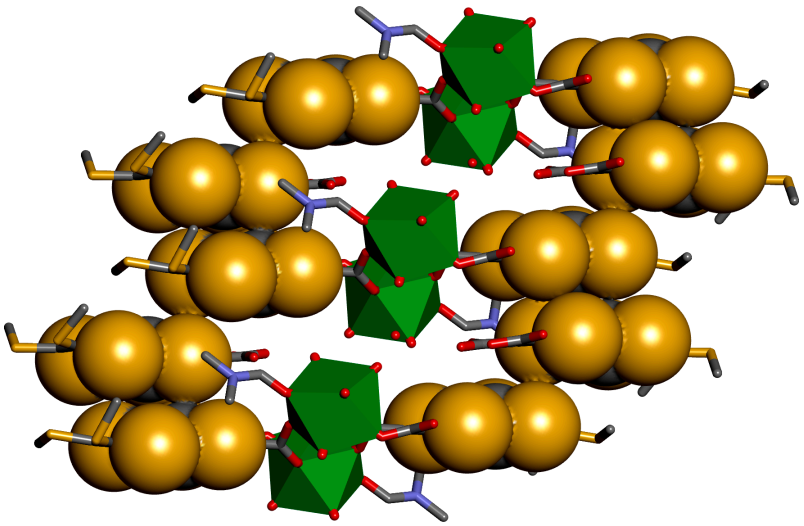

Figure 2. Packing along the *a* direction of the TTF moieties. The van der Waals surface of the TTF cores of the coordinated and non-coordinated TTFs are represented while coordination polyhedra of Yb^{III} are also shown (in green).

$\chi_M T$ *vs.* T (with χ_M the molar magnetic susceptibility and T the temperature in Kelvin) decreases monotonically on cooling from 2.40 $cm^3 \cdot K \cdot mol^{-1}$ at room temperature down to 0.99 $cm^3 \cdot K \cdot mol^{-1}$ at 2 K due to the thermal population of crystal field levels within the ground state multiplet $^2F_{7/2}$ (Figure S8). Concomitantly, the M *vs.* H curve saturates around 1.5 Nβ at 2 K (Figure S8). It must be mentioned that no interaction between Yb^{III} can be detected down to 2 K. Rotating single-crystal magnetometry performed at 2 K allows the determination of magnetic axes. A platelet-shaped single-crystal is rotated in a field of 1 kOe in three perpendicular planes (Figure S9) of the crystal reference frame (XYZ) and the magnetization recorded as a function of the angle (θ) between the magnetic field and the initial position. The molar magnetic susceptibility was fitted with:

$$\chi_M T = \frac{MT}{H} = \chi_{\alpha\alpha}\cos^2\theta + \chi_{\beta\beta}\sin^2\theta + 2\chi_{\alpha\beta}\sin\theta\cos\theta \quad (1)$$

where α and β are the directions X, Y, and Z, and θ is the angle between H and α. After simultaneous least-square fitting of the three curves on Figure 3 the susceptibility tensor in the crystal frame (XYZ) is:

$$\chi_M T = \begin{pmatrix} 1.418 & 0.320 & -0.203 \\ 0.320 & 1.223 & -0.173 \\ -0.203 & -0.173 & 0.270 \end{pmatrix} cm^3 \cdot K \cdot mol^{-1} \quad (2)$$

The principal values and direction of the susceptibility tensor in the XYZ crystal frame are then given by:

$$\chi_{xx} T \begin{pmatrix} 0.602 \\ -0.798 \\ 0.022 \end{pmatrix} = 0.986,\ \chi_{yy} T \begin{pmatrix} -0.132 \\ -0.127 \\ -0.983 \end{pmatrix} = 0.220,\ \chi_{zz} T \begin{pmatrix} 0.787 \\ 0.589 \\ -0.182 \end{pmatrix} = 1.70\ cm^3 \cdot K \cdot mol^{-1} \quad (3)$$

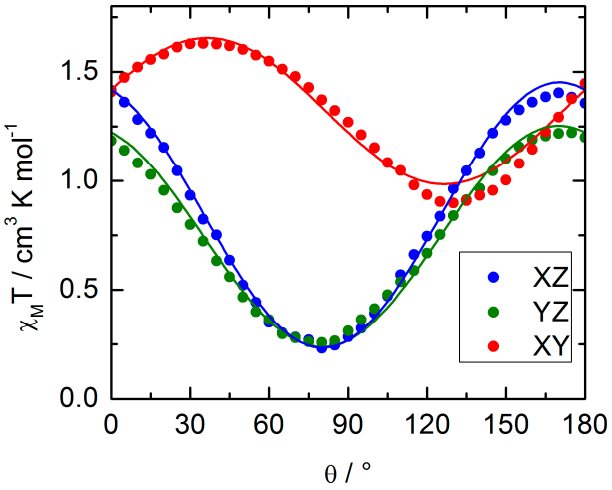

Figure 3. Angular dependence of $\chi_M T$ of a single crystal rotated in three perpendicular planes with H = 10 kOe at 2 K. Best fitted curves are in full lines.

In the effective spin ½ approximation the principal g-values are g_x = 3.24, g_y = 1.53, and g_z = 4.25. Clearly, the anisotropy is more planar than axial. This is in contradiction with what has been observed in 8-coordinated Yb^{III} complexes in which g_z is much larger than the two other components [31]. This is probably due to the peculiar environment around the Yb^{III} ion. The orientation of the g-tensor with respect to the molecular axes is represented on Figure 4. g_z almost coincides with the four-fold axis of the square antiprism while g_x and g_y reside in the perpendicular plane. We tentatively tried to reproduce these static magnetic properties using the *ab initio* CASSCF/PT2/SI-SO approach (see computational details). Unfortunately, all tentative efforts failed to properly reproduce the magnetic susceptibility and magnetization curves (Figure S8). This underlines the difficulties already observed in the literature to efficiently model both the wavefunction and the energy of the low-lying multiplets of Yb^{III} based SMM. Indeed, whereas for Dy^{III} complexes it is admitted that a CASSCF/SI-SO approach correctly describes the magnetic behavior, for Yb^{III} molecules, examples exist where a CASSCF/SI-SO is sufficient [6]; however, adding dynamical correlation through a PT2 treatment is mandatory in some other cases [31]. Ultimately, the present **Yb** complex joined the $Yb(Murex)_3$ complex in the list of complexes for which the *ab initio* procedure dramatically failed [32,33]. At this stage, no clear explanation exists even if one may tentatively and non-exhaustively cite (i) the number of 4f electrons; (ii) the importance of dynamical correlation; and (iii) the propensity of having Yb^{III}/Yb^{II} mixing in the ground-state wave function. In the present case, one may also ascribe the encountered computational difficulty to (i) the model used to describe the 1D chain, and (ii) the problem related to the influence of the water molecule [11]. However, several different models (not described here) have been tested to take into account the 1-D architecture and the presence of water molecules, but with no clear improvements in the calculated results compared to the experiment. Works are still in progress to elucidate this observed peculiar behavior and, more generally, the way Yb-based SMM have to be computationally described.

As expected from single-crystal rotating magnetometry, no slow relaxation of the magnetization can be detected in the absence of an external field at any temperature. This is in line with previous reports on Yb^{III}-based complexes [32]. At 2 K the relaxation is slowest at the optimum field equal to 1 kOe. The frequency dependences of the in-phase and out-of-phasesuc component of the AC susceptibility are represented on Figure 5 between 1.8 and 6 K. The temperature dependence of the relaxation time extracted (extended Debye model, ESI, Table S4) from the frequency scan at fixed temperatures is represented on Figure 5. Different relaxation processes may operate: (1) Orbach; (2) Raman; (3) direct and quantum tunneling. The first two are thermally-dependent and the last one is temperature-independent. Clearly the relaxation is thermally-activated. However, the

experimental data can only be reproduced with two Arrhenius profiles which correspond to two Orbach processes ($\tau^{-1} = {\tau_1}^{-1} \exp(-\Delta_1/T) + {\tau_2}^{-1} \exp(-\Delta_2/T)$) above and below 3 K with $\tau_1 = 3.3(9) \times 10^{-7}$ s, $\Delta_1 = 28(1)$ K, $\tau_2 = 2.0(2) \times 10^{-4}$ s, and $\Delta_2 = 3.2(3)$ K (Figure 5). Deviation from a single Arrhenius law is commonly observed in Yb^{III}-based SMMs [5,7,9] but had never been quantitatively analyzed.

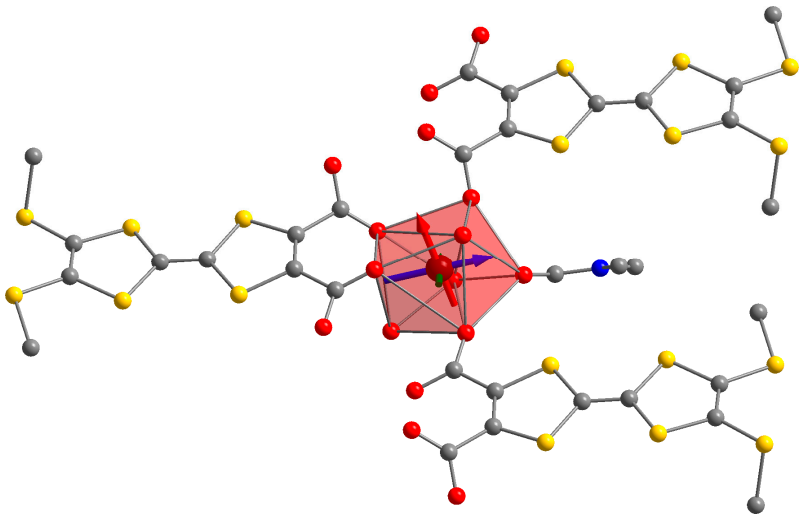

Figure 4. Principal magnetic axes (g_x: blue, g_y: green, g_z: red) of **Yb**.

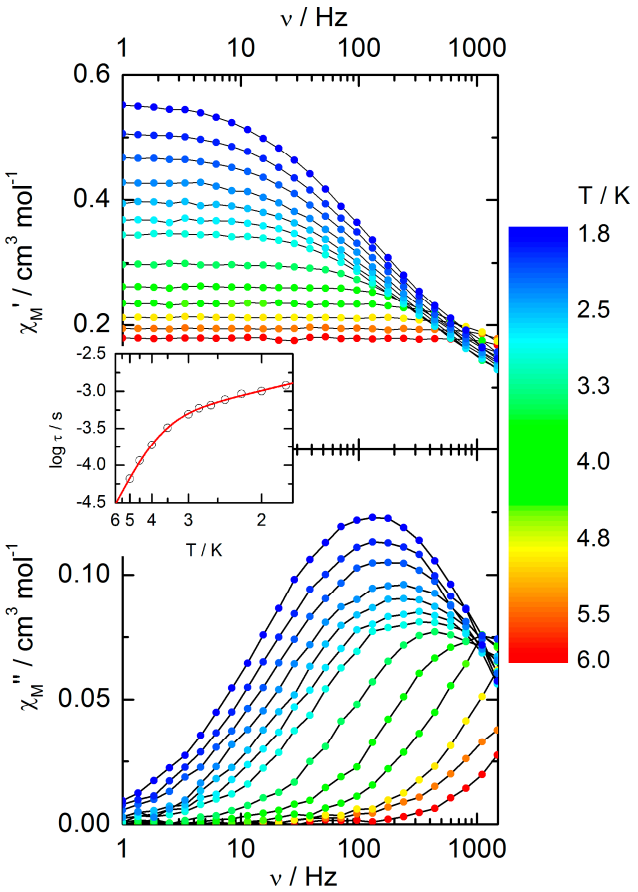

Figure 5. Frequency dependences of the in-phase (χ_M') and out-of-phase (χ_M'') components of the ac susceptibility measured between 1.8 and 6 K in an external DC field of 1 kOe. Insert: temperature dependence of the relaxation time with the best-fitted curve (see text).

In summary, we have synthesized a mono-dimensional coordination polymer of Yb^{III} thanks to the redox-active deprotonated 4,5-bis(carboxylic)-4′,5′-methyldithiotetrathiafulvene bridges. To date, **Yb** is the unique example of Yb^{III}-based coordination polymer that displays slow magnetic relaxation. **Yb** highlights the important role played by the carboxylate functions in generating a mono-dimensional coordination polymer. The resulting organization of the ligands around the Yb^{III} ion induces SMM behavior with unusual planar magnetic anisotropy. The presence of the tetrathiafulvalene core guaranties the redox activity of the polymer as well as the opening of new possibilities of multi-property coordination complexes.

3. Materials and Methods

3.1. Synthesis. General Procedures, and Materials

The precursor $Yb(hfac)_3 \cdot 2H_2O$ ($hfac^-$ = 1,1,1,5,5,5-hexafluoroacetylacetonate anion) and the ligand $\mathbf{Na_2L}$ were synthesized following previously reported methods [34,35]. All other reagents were commercially available and used without further purification.

*3.2. Synthesis of Complex {[Yb(**L**)(H$_2$O)$_3$(DMF)]· (**HL**)· (H$_2$O)}$_n$ (**Yb**)*

0.115 mmol of $Yb(hfac)_3 \cdot 2H_2O$ (97 mg) and 0.115 mmol of $\mathbf{Na_2L}$ were dissolved in 15 mL of DMF. After 15 min of stirring, the solution was put in a test tube and then water was layered at room temperature in the dark. After two weeks of slow diffusion, red-brown single crystals which are suitable for X-ray studies are obtained. Yield 20 mg (16%) based on the metallic precursor. Anal. Calcd (%) for $C_{23}H_{22}N_1O_{13}S_{12}Yb_1$: C 25.63, H 2.04, N 1.30; found: C 26.69, H 2.12, N 1.27.

3.3. Crystallography

A single crystal of {[**Yb**(**L**)$(H_2O)_3$(DMF)]· (**HL**)· $(H_2O)\}_n$ was mounted on a APEXII Bruker-AXS diffractometer for data collection (MoK_α radiation source, λ = 0.71073 Å) at the Centre de Diffractométrie (CDFIX), Université de Rennes 1, France. The structure was solved by direct methods using the SIR-97 program and refined with a full matrix least-squares method on F^2 using the SHELXL-97 program [36,37]. Crystallographic data are summarized in Table S1. Complete crystal structure results as a CIF file including bond lengths, angles, and atomic coordinates are included as Supporting Information. The CCDC number is 1471405 for compound **Yb**.

3.4. Physical Measurements

The elementary analyses of the compound were performed at the Centre Régional de Mesures Physiques de l'Ouest, Rennes. Cyclic voltametry was carried out in CH_2Cl_2 solution, containing 0.1 M $N(C_4H_9)_4PF_6$ as the supporting electrolyte. Voltamograms were recorded at 100 $mV \cdot s^{-1}$ at a platinum disk electrode. The potentials were measured *versus* a saturated calomel electrode (SCE). Absorption spectra were recorded on a Varian Cary 5000 UV-Visible-NIR spectrometer equipped with an integration sphere. The DC magnetic susceptibility measurements were performed on solid polycrystalline sample with a Quantum Design MPMS-XL SQUID magnetometer between 2 and 300 K in an applied magnetic field of 0.2 T for temperatures in the range 2–20 K and 1 T for temperatures between 20 and 300 K. These measurements were all corrected for the diamagnetic contribution as calculated with Pascal's constants. Single crystal magnetization measurements have been performed on an oriented single crystal (using X-ray diffraction) with the same Quantum Design MPMS-XL SQUID magnetometer equipped with a rotator which allows the crystal to rotate within a plane. Magnetization has been recorded at 2 K within a field of 10 kOe.

3.5. Computational Details

DFT geometry optimizations and TD-DFT excitation energy calculations of the ligand $\mathbf{H_2L}$ were carried out with the Gaussian 09 (revision A.02) package [38] employing the PBE0 hybrid

functional [39,40]. The "Stuttgart/Dresden" basis sets and effective core potentials were used to describe the yttrium atom [41], whereas all other atoms were described with the SVP basis sets [42]. The first 50 monoelectronic excitations were calculated. In all steps, a modeling of bulk solvent effects (solvent = dichloromethane) was included through the Polarizable Continuum Model (PCM) [43], using a linear-response non-equilibrium approach for the TD-DFT step [44,45]. Molecular orbitals were sketched using the Gabedit graphical interface [46].

Wavefunction-based calculations were carried out on a model structure of the Yb^{III}-based coordination polymer **Yb** (see below) by using the SA-CASSCF/PT2/SI-SO approach, as implemented in the MOLCAS quantum chemistry package (versions 7.8) [47]. In this approach, the relativistic effects are treated in two steps on the basis of the Douglas-Kroll Hamiltonian. First, the scalar terms were included in the basis-set generation and were used to determine the spin-free wavefunctions and energies in the complete active space self-consistent field (CASSCF) method [48]. Next, spin-orbit coupling was added within the restricted-active-space-state-interaction (RASSI-SO) method, which uses the spin-free wavefunctions as basis states [49,50]. The resulting wavefunctions and energies were corrected with dynamical correlation using the complete active space second-order perturbation (CASPT2) method and are then used to compute the magnetic properties and g-tensors of the lowest states from the energy spectrum by using the pseudo-spin $S = 1/2$ formalism in the SINGLE-ANISO routine [51,52]. Cholesky decomposition of the bielectronic integrals was employed to save disk space and speed up the calculations [53]. The computational model consisted of three Yb(DMF)(**L**)$(H_2O)_3$ units (Figure S10). The atomic positions were extracted from the X-ray crystal structures. The $S_2(C_2)(SCH_3)_2$ moieties of the TTF-derived ligands were replaced by hydrogen atoms, as well as the two CH_3 groups coordinated to the N atom of the DMF ligands. The active space of the self consistent field (CASSCF) method consisted of the thirteen 4f electrons of the Yb^{III} ion spanning the seven 4f orbitals, *i.e.*, CAS(13,7)SCF. State-averaged CASSCF calculations were performed for all of the doublet states (seven roots). All atoms were described by ANO-RCC basis sets [54–56]. The following contractions were used: [8s7p4d3f2g] for the central Yb atom; [6s5p3d] for the two neighboring Yb atoms which were replaced by Yb atoms; [4s3p2d] for the O atoms directly coordinated to Yb atom; [3s2p1d] for the C and O atoms bridging the Yb atom to the Y atoms; [4s3p] for the S atoms; [3s2p] for the remaining C, N, and O atoms and [2s] for the H atoms.

Supplementary Materials: The following are available online at www.mdpi.com/2312-7481/2/2/26/s1, Figure S1: (a) Crystal packing of **Yb** highlighting the interactions with the $\mathbf{HL}^-$ counter anions through the S ... S short contacts; (b) Representation of the S ... S short contacts between the $\mathbf{HL}^-$ mono-anions; Figure S2: (a) Experimental UV-visible absorption spectra in CH_2Cl_2 solution of $\mathbf{H_2L}$ ($C = 4 \times 10^{-5}$ mol·L^{-1}) (open gray circles). Respective Gaussian decompositions (dashed lines) and best fit (full black line) (R = 0.99957); (b) Theoretical absorption spectra of compounds $\mathbf{H_2L}$ (black line). The sticks represent the mean contributions of the absorption spectra; Figure S3: Experimental solid-state UV-visible absorption spectrum (open circles) for $\mathbf{H_2L}$ at room temperature with respective Gaussian decompositions (dashed coloured lines) and best fit (full black line) R = 0.99814; Figure S4: Experimental solid-state UV-visible absorption spectrum (open circles) for $\mathbf{Na_2L}$ at room temperature with respective Gaussian decompositions (dashed coloured lines) and best fit (full black line) R = 0.99893; Figure S5: MO diagram of $\mathbf{H_2L}$. Energy levels of the centered TTF donor and carboxylic acceptor are represented in orange and blue color, respectively; Figure S6: Experimental solid-state UV-visible absorption spectrum (open circles) for **Yb** at room temperature with respective Gaussian decompositions (dashed coloured lines) and best fit (full black line) R = 0.99875; Figure S7: Cyclic voltametry of **Yb** in CH_2Cl_2 at a scan rate of 100 mV.s^{-1}.The potentials were measured *versus* a saturated calomel electrode (SCE); glassy carbon as the working electrode; Pt wire as the counter electrodes; Figure S8: Temperature dependence of $\chi_M T$ for **Yb**. Inset: magnetic field dependence of the magnetization for **Yb** recorded at 2 K. Full red lines correspond to the *ab initio* simulated curves; Figure S9: Oriented single crystal of **Yb** with the XYZ crystal reference frame; Figure S10: Model used in the CASSCF/PT2/SI-SO calculations. Oxygen atoms are in red, nitrogen in blue, carbon in grey, sulphur in yellow and hydrogen in white. Table S1: X-ray crystallographic data for **Yb**; Table S2: TD-DFT calculated excitation energies and main compositions of the low-lying electronic transitions for $\mathbf{H_2L}$. In addition, the charge transfers and the pure intramolecular transitions are reported. ID and H, L represent the intramolecular TTF (Donor) and the HOMO, the LUMO, respectively. ILCT corresponds to Intra-Ligand Charge Transfer. The theoretical values are evaluated at the PCM(CH_3OH)-PBE0/SVP level of approximation; Table S3: Solid-state absorption data for ligands $\mathbf{H_2L}$, $Na_2\mathbf{L}$, and the coordination complex **Yb**; Table S4: Best fitted parameters (χ_T, χ_S, τ and α) with the extended Debye model **Yb** at 1 kOe in the temperature range 1.8–5 K.

Acknowledgments: This work was supported by the CNRS, Rennes Métropole, Université de Rennes 1, and Agence Nationale de la Recherche (No. ANR-13-BS07-0022-01).

Author Contributions: A.B.J. performed the syntheses and crystallizations; S.G. performed the single crystal X-ray diffraction experiments and structure refinements; O.C. performed the magnetic measurements and analyses. J.J. performed the ab intio calculations. F.P., O.C. and B.L.G. conceived and designed the experiments and contributed equally to the writing of the article.

Conflicts of Interest: The authors declare no conflict of interest. The founding sponsors had no role in the design of the study; in the collection, analyses, or interpretation of data; in the writing of the manuscript, and in the decision to publish the results.

Abbreviations

The following abbreviations are used in this manuscript:

SMM	Single Molecule Magnet
TTF	TetraThiaFulvalene
DMF	DiMethylFormamide
Hfac	1,1,1,5,5,5-hexafluoroacetylacetonate
DFT	Density Functional Theory
TD-DFT	Time Dependent Density Functional Theory
ILCT	Intra-Ligand Charge Transfer
HOMO	Highest Occupied Molecular Orbital
LUMO	Lowest Unoccupied Molecular Orbital
ID	Intra Donor
PCM	Polarizable Continuum Model
CASSCF	Complete Active Space Self-Consistent Field
RASSI-SO	Restricted Active Space State Interaction—Spin-Orbit

References

1. Sessoli, R.; Powell, A.K. Strategies towards single molecule magnets based on lanthanide ions. *Coord. Chem. Rev.* **2009**, *253*, 2328–2341. [CrossRef]
2. Rinehart, J.D.; Long, J.R. Exploiting single-ion anisotropy in the design of f-element single-molecule magnets. *Chem. Sci.* **2011**, *2*, 2078–2085. [CrossRef]
3. Woodruff, D.N.; Winpenny, R.E.P.; Layfield, R.A. Lanthanide Single-Molecule Magnets. *Chem. Rev.* **2013**, *113*, 5110, and references therein. [CrossRef] [PubMed]
4. Boulon, M.E.; Cucinotta, G.; Luzon, J.; Degl'Innocenti, C.; Perfetti, M.; Bernot, K.; Calvez, G.; Caneschi, A.; Sessoli, R. Magnetic Anisotropy and Spin-Parity Effect Along the Series of Lanthanide Complexes with DOTA. *Angew. Chem. Int. Ed.* **2013**, *52*, 350–354. [CrossRef] [PubMed]
5. Pointillart, F.; Le Guennic, B.; Golhen, S.; Cador, O.; Maury, O.; Ouahab, L. A redox-active luminescent ytterbium based single molecule magnet. *Chem. Commun.* **2013**, *49*, 615–617. [CrossRef] [PubMed]
6. Liu, J.L.; Yuan, K.; Leng, J.D.; Ungur, L.; Wernsdorfer, W.; Guo, F.S.; Chibotaru, L.F.; Tong, M.L. A Six-Coordinate Ytterbium Complex Exhibiting Easy-Plane Anisotropy and Field-Induced Single-Ion Magnet Behavior. *Inorg. Chem.* **2012**, *51*, 8538–8544. [CrossRef] [PubMed]
7. Li, Q.-W.; Liu, J.-L.; Jia, J.-H.; Chen, Y.-C.; Liu, J.; Wang, L.-F.; Tong, M.-L. "Half-sandwich" Yb^{III} single-ion magnets with metallacrowns. *Chem. Commun.* **2015**, *51*, 10291–10294. [CrossRef] [PubMed]
8. Lannes, A.; Luneau, D. New Family of Lanthanide-Based Complexes with Different Scorpionate-Type Ligands: A rare Case Where Dysprosium and Ytterbium Analogues Display Single-Ion-Magnet Behavior. *Inorg. Chem.* **2015**, *54*, 6736–6743. [CrossRef] [PubMed]
9. Pedersen, K.S.; Dreiser, J.; Weihe, H.; Sibille, R.; Johannesen, H.V.; Sorensen, M.A.; Nielsen, B.E.; Sigrist, M.; Mutka, H.; Rols, S.; Bendix, J.; Piligkos, S. Design of Single-Molecule Magnets: Insufficiency of the Anisotropy Barrier as the Sole Criterion. *Inorg. Chem.* **2015**, *54*, 7600–7606. [CrossRef] [PubMed]

10. Long, J.; Vallat, R.; Ferreira, R.A.S.; Carlos, L.D.; Almeida Paz, F.A.; Guari, Y.; Larionova, J. A bifunctional luminescent single-ion magnet: Towards correlation between luminescence studies and magnetic slow relaxation processes. *Chem. Commun.* **2012**, *48*, 9974–9976. [CrossRef] [PubMed]
11. Cucinotta, G.; Perfetti, M.; Luzon, J.; Etienne, M.; Car, P.E.; Caneschi, A.; Calvez, G.; Bernot, K.; Sessoli, R. Magnetic Anisotropy in a Dysprosium/DOTA Single-Molecule Magnet: Beyond Simple Magneto-Structural Correlations. *Angew. Chem. Int. Ed.* **2012**, *51*, 1606–1610. [CrossRef] [PubMed]
12. Pointillart, F.; Le Guennic, B.; Cador, O.; Maury, O.; Ouahab, L. Lanthanide Ion and Tetrathiafulvalene-Based Ligand as a "magic" Couple toward Luminescence, Single Molecule Magnets, and Magnetostructural Correlations. *Acc. Chem. Res.* **2015**, *48*, 2834–2842, and references therein. [CrossRef] [PubMed]
13. Lin, S.-Y.; Wang, C.; Zhao, L.; Wua, J.; Tang, J. Chiral mononuclear lanthanide complexes and the field-induced single-ion magnet behaviour of a Dy analogue. *Dalton Trans.* **2015**, *44*, 223–229. [CrossRef] [PubMed]
14. Long, J.; Rouquette, J.; Thibaud, J.-M.; Ferreira, R.A.S.; Carlos, L.D.; Donnadieu, B.; Vieru, V.; Chibotaru, L.F.; Konczewicz, L.; Haines, J.; Guari, Y.; Larionova, J. A high-temperature molecular ferroelectric Zn/Dy complex exhibiting single-ion-magnet behaviour and lanthanide luminescence. *Angew. Chem. Int. Ed.* **2015**, *54*, 2236–2240. [CrossRef] [PubMed]
15. Batail, P., Ed.; *Molecular Conductors*; ACS: Washington, DC, USA, 2004; Volume 104, pp. 4887–5782 and references therein.
16. Lorcy, D.; Bellec, N.; Fourmigue, M.; Avarvari, N. Tetrathiafulvalene-based group XV ligands: Synthesis, coordination chemistry and radical cation salts. *Coord. Chem. Rev.* **2009**, *253*, 1398–1438, and references therein. [CrossRef]
17. Pointillart, F.; Golhen, S.; Cador, O.; Ouahab, L. Paramagnetic 3d coordination complexes involving redox-active tetrathiafulvalene derivatives: an efficient approach to elaborate multi-properties materials. *Dalton Trans.* **2013**, *42*, 1949–1960 and references therein. [CrossRef] [PubMed]
18. Ebihara, M.; Nomura, M.; Sakai, S.; Kawamura, T. Synthesis, structure and properties of TTF-carboxylate bridged paddlewheel dirhodium complexes, $Rh_2(ButCO_2)_3(TTFCO_2)$ and $Rh_2(ButCO_2)_2(TTFCO_2)_2$. *Inorg. Chim. Acta* **2007**, *360*, 2345–2352. [CrossRef]
19. Gu, J.; Zhu, Q.-Y.; Zhang, Y.; Lu, W.; Niu, G.-Y.; Dai, J. Metal Co(II) and Ni(II) coordination compounds with tetrathiafulvalene carboxylate. *Inorg. Chem. Commun.* **2008**, *11*, 175–178. [CrossRef]
20. Han, Y.-F.; Li, X.-Y.; Li, J.-K.; Zheng, Z.-B.; Wu, R.T.; Lu, J.-R. Synthesis and Structure Characterization of $Zn(TC\text{-}TTF)_{0.5}(bipy)_2(CH_3OH)$. *Chin. J. Inorg. Chem.* **2009**, *25*, 1290–1294.
21. Qin, Y.-R.; Zhu, Q.-Y.; Huo, L.-B.; Shi, Z.; Bian, G.-Q.; Dai, J. Tetrathiafulvalene-Tetracarboxylate: An Intriguing Building Block with Versatility in Coordination Structures and Redox Properties. *Inorg. Chem.* **2010**, *49*, 7372–7381. [CrossRef] [PubMed]
22. Nguyen, T.L.A.; Devic, T.; Mialane, P.; Rivière, E.; Sonnauer, A.; Stock, N.; Demir-Cakan, R.; Morcrette, M.; Livage, C.; Marrot, J.; Tarascon, J.-M.; Férey, G. Reinvestigation of the MII (M = Ni, Co)/TetraThiafulvaleneTetraCarboxylate System Using High-Throughput Methods: Isolation of a Molecular Complex and Its Single-Crystal-to-Single-Crystal Transformation to a Two-Dimensional Coordination Polymer. *Inorg. Chem.* **2010**, *49*, 10710–10717. [CrossRef] [PubMed]
23. Nguyen, T.L.H.; Demir-Cakan, R.; Devic, T.; Morcrette, M.; Ahnfeldt, T.; Auban-Senzier, P.; Stock, N.; Goncalves, A.-M.; Filinchuk, Y.; Tarascon, J.-M.; Férey, G. 3-D Coordination Polymers Based on the Tetrathiafulvalenetetracarboxylate (TTF-TC) Derivative: Synthesis, Characterization, and Oxidation Issues. *Inorg. Chem.* **2010**, *49*, 7135–7143. [CrossRef] [PubMed]
24. Han, Q.-H.; Shi, Z.; Shao, M.-Y.; Li, X.-Y.; Zhu, Q.-Y.; Dai, J. Mg(II) and Zn(II) tetrathiafulvalene bicarboxylates with hydrogen-bond-assembled band-like supramolecular structures. *Inorg. Chem. Commun.* **2012**, *15*, 190–193. [CrossRef]
25. Smucker, B.W.; Bacsa, J.; Bera, J.K.; Reinheimer, E.W. Redox-active TTF carboxylate as an axial bridging ligand for dirhenium metal–metal bonded complexes. *Inorg. Chim. Acta* **2015**, *425*, 233–238. [CrossRef]
26. Faulkner, S.; Burton-Pye, B.P.; Khan, T.; Martin, L.R.; Wray, S.D.; Skabara, P.J. Interaction between tetrathiafulvalene carboxylic acid and ytterbium DO3A: Solution state self-assembly of a ternary complex which is luminescent in the near IR. *Chem. Commun.* **2002**, 1668–1669. [CrossRef]

27. Pointillart, F.; Le Gal, Y.; Golhen, S.; Cador, O.; Ouahab, L. Binuclear gadolinium(III) coordination complex based on bridging tetrathiafulvalenecarboxylate radical cations. *Chem. Commun.* **2009**, *25*, 3777–3779. [CrossRef] [PubMed]
28. Llunell, M.; Casanova, D.; Cirera, J.; Bofill, J.M.; Alemany, P.; Alvarez, S. *SHAPE (Version 2.1)*; Universitat de Barcelona: Barcelona, Spain, 2013.
29. Cosquer, G.; Pointillart, F.; Le Guennic, B.; Le Gal, Y.; Golhen, S.; Cador, O.; Ouahab, L. 3d4f Heterobimetallic Dinuclear and Tetranuclear Complexes Involving Tetrathiafulvalene as Ligands: X-ray Structures and Magnetic and Photophysical Investigations. *Inorg. Chem.* **2012**, *51*, 8488–8501. [CrossRef] [PubMed]
30. D'Aléo, A.; Pointillart, F.; Ouahab, L.; Andraud, C.; Maury, O. Charge transfer excited states sensitization of lanthanide emitting from the visible to the near-infra-red. *Coord. Chem. Rev.* **2012**, *256*, 1604–1620. [CrossRef]
31. Jung, J.; da Cunha, T.T.; Le Guennic, B.; Pointillart, F.; Pereira, C.L.M.; Luzon, J.; Golhen, S.; Cador, O.; Maury, O.; Ouahab, L. Magnetic Studies of Redox Active Tetrathiafulvalene-Based Complexes: Dysprosium *versus* Ytterbium Analogues. *Eur. J. Inorg. Chem.* **2014**, *2014*, 3888–3894. [CrossRef]
32. Yi, X.; Bernot, K.; Le Corre, V.; Calvez, G.; Pointillart, F.; Cador, C.; Le Guennic, B.; Jung, J.; Maury, O.; Placide, V.; *et al.* Unraveling the crystal Structure of Lanthanide-Murexide Complexes: Use of an Ancient Complexometry Indicator as a Near-Infrared-Emitting Single-Ion Magnet. *Chem. Eur. J.* **2014**, *20*, 1569–1576. [CrossRef] [PubMed]
33. Pointillart, F.; Jung, J.; Berraud-Pache, R.; Le Guennic, B.; Dorcet, V.; Golhen, S.; Cador, O.; Maury, O.; Decurtins, S.; Liu, S.-X.; *et al.* Luminescence and Single Molecule Magnet Behavior in Lanthanide Complexes Involving A Tetrathiafulvalene-Fused Dipyridophenazine Ligand. *Inorg. Chem.* **2015**, *54*, 5384–5397. [CrossRef] [PubMed]
34. Richardson, M.F.; Wagner, W.F.; Sands, D.E. Rare-earth trishexafluoroacetylacetonates and related compounds. *J. Inorg. Nucl. Chem.* **1968**, *30*, 1275–1289. [CrossRef]
35. Lin, H.; Yan, Z.; Dai, J.; Zhang, D.; Zuo, J.; Zhu, Q.; Jia, D. A water-soluble derivative of tetrathiafulvalene exhibiting pH sensitive redox properties. *New J. Chem.* **2005**, *29*, 509–513. [CrossRef]
36. Sheldrick, G.M. *SHELX97—Programs for Crystal Structure Analysis (Release 97-2)*; Institüt für Anorganische Chemie der Universität: Göttingen, Germany, 1998.
37. Altomare, A.; Burla, M.C.; Camalli, M.; Cascarano, G.L.; Giacovazzo, C.; Guagliardi, A.; Moliterni, A.G.G.; Polidori, G.; Spagna, R. SIR97: A new tool for crystal structure determination and refinement. *J. Appl. Cryst.* **1999**, *32*, 115–119. [CrossRef]
38. Frisch, M.J.; Trucks, G.W.; Schlegel, H.B.; Scuseria, G.E.; Robb, M.A.; Cheeseman, J.R.; Scalmani, G.; Barone, V.; Mennucci, B.; Petersson, G.A.; *et al. Gaussian 09 Revision A.02*; Gaussian Inc.: Wallingford, CT, USA, 2009.
39. Perdew, J.P.; Burke, K.; Ernzerhof, M. Generalized Gradient Approximation Made Simple. *Phys. Rev. Lett.* **1996**, *77*, 3865–3868. [CrossRef] [PubMed]
40. Adamo, C.; Barone, V. Toward reliable density functional methods without adjustable parameters: The PBE0 model. *J. Chem. Phys.* **1999**, *110*, 6158–6170. [CrossRef]
41. Dolg, M.; Stoll, H.; Preuss, H. A combination of quasirelativistic pseudopotential and ligand field calculations for lanthanoid compounds. *Theor. Chim. Acta* **1993**, *85*, 441–450. [CrossRef]
42. Weigend, F.; Ahlrichs, R. Balanced basis sets of split valence, triple zeta valence and quadruple zeta valence quality for H to Rn: Design and assessment of accuracy. *Phys. Chem. Chem. Phys.* **2005**, *7*, 3297–3305. [CrossRef] [PubMed]
43. Tomasi, J.; Mennucci, B.; Cammi, R. Quantum Mechanical Continuum Solvation Models. *Chem. Rev.* **2005**, *105*, 2999–3094. [CrossRef] [PubMed]
44. Cossi, M.; Barone, V. Quantum Mechanical Continuum Solvation Models. *J. Chem. Phys.* **2001**, *115*, 4708–4717. [CrossRef]
45. Improta, R.; Barone, V.; Scalmani, G.; Frisch, M.J. A state-specific polarizable continuum model time dependent density functional theory method for excited state calculations in solution. *J. Chem. Phys.* **2006**, *125*, 054103. [CrossRef] [PubMed]
46. Allouche, A.-R. Gabedit—A graphical user interface for computational chemistry softwares. *J. Comput. Chem.* **2011**, *32*, 174–182. [CrossRef] [PubMed]
47. Aquilante, F.; De Vico, L.; Ferré, N.; Ghigo, G.; Malmqvist, P.-A.; Neograd y, P.; Bondo Pedersen, T.; Pitonak, M.; Reiher, M.; Roos, B.O.; *et al.* MOLCAS 7: The Next Generation. *J. Comput. Chem.* **2010**, *31*, 224–247. [CrossRef] [PubMed]

48. Roos, B.O.; Taylor, P.R.; Siegbahn, P.E.M. A complete active space SCF method (CASSCF) using a density matrix formulated super-CI approach. *Chem. Phys.* **1980**, *48*, 157–173. [CrossRef]
49. Malmqvist, P.Å.; Roos, B.O.; Schimmelpfennig, B. The restricted active space (RAS) state interaction approach with spin-orbit coupling. *Chem. Phys. Lett.* **2002**, *357*, 230–240. [CrossRef]
50. Malmqvist, P.-Å.; Roos, B.O. The CASSCF state interaction method. *Chem. Phys. Lett.* **1989**, *155*, 189–194. [CrossRef]
51. Chibotaru, L.F.; Ungur, L. Ab initio calculation of anisotropic magnetic properties of complexes. I. Unique definition of pseudospin Hamiltonians and their derivation. *J. Chem. Phys.* **2012**, *137*, 064112. [CrossRef] [PubMed]
52. Chibotaru, L.; Ungur, L.; Soncini, A. The Origin of Nonmagnetic Kramers Doublets in the Ground State of Dysprosium Triangles: Evidence for a Toroidal Magnetic Moment. *Angew. Chem., Int. Ed.* **2008**, *47*, 4126–4129. [CrossRef] [PubMed]
53. Aquilante, F.; Malmqvist, P.-Å.; Pedersen, T.B.; Ghosh, A.; Roos, B.O. Cholesky Decomposition-Based Multiconfiguration Second-Order Perturbation Theory (CD-CASPT2): Application to the Spin-State Energetics of Co^{III}(diiminato)(NPh). *J. Chem. Theory Comput.* **2008**, *4*, 694–702. [CrossRef] [PubMed]
54. Roos, B.O.; Lindh, R.; Malmqvist, P.-A.; Veryazov, V.; Widmark, P.-O. Main Group Atoms and Dimers Studied with a New Relativistic ANO Basis Set. *J. Phys. Chem. A* **2004**, *108*, 2851–2858. [CrossRef]
55. Roos, B.O.; Lindh, R.; Malmqvist, P.-A.; Veryazov, V.; Widmark, P.-O. New Relativistic ANO Basis Sets for Transition Metal Atoms. *J. Phys. Chem. A* **2005**, *109*, 6575–6579. [CrossRef] [PubMed]
56. Roos, B.O.; Lindh, R.; Malmqvist, P.-Å.; Veryazov, V.; Widmark, P.-O.; Borin, A.C. New Relativistic Atomic Natural Orbital Basis Sets for Lanthanide Atoms with Applications to the Ce Diatom and LuF_3. *J. Phys. Chem. A* **2008**, *112*, 11431–11435. [CrossRef] [PubMed]